Journal of Catalysis 281 (2011) 106–118

Contents lists available at ScienceDirect

Journal of Catalysis

journal homepage: www.elsevier.com/locate/jcat

Heteroepitaxial growth of gold on flowerlike magnetite: An efficacious and magnetically recyclable catalyst for chemoselective hydrogenation of crotonaldehyde to crotyl alcohol

Yuan Zhu[a], Li Tian[a], Zheng Jiang[b], Yan Pei[a,*], Songhai Xie[a], Minghua Qiao[a,*], Kangnian Fan[a]

[a] *Department of Chemistry and Shanghai Key Laboratory of Molecular Catalysis and Innovative Materials, Fudan University, Shanghai 200433, PR China*
[b] *Shanghai Synchrotron Radiation Facility, Shanghai Institute of Applied Physics, Chinese Academy of Sciences, Shanghai 201204, PR China*

ARTICLE INFO

Article history:
Received 12 January 2011
Revised 11 April 2011
Accepted 12 April 2011
Available online 6 May 2011

Keywords:
Au/Fe_3O_4
Heteroepitaxial growth
Crotonaldehyde
Crotyl alcohol
Hydrogenation
Perimeter interface

ABSTRACT

Au/Fe_3O_4 catalysts with flowerlike and particulate morphologies have been prepared by homogeneous deposition–precipitation of gold on hematite materials synthesized in different ways, followed by integrative reduction. HRTEM revealed the heteroepitaxial growth of gold crystallites on flowerlike magnetite materials along the {1 1 1} planes, which may account for their smaller and more uniform gold nanoparticles. The stronger metal-support interaction on flowerlike Au/Fe_3O_4 catalysts was also manifested by the higher reduction temperature of gold than that on particulate magnetite-supported catalysts. In liquid phase hydrogenation of crotonaldehyde, the flowerlike Au/Fe_3O_4 catalysts show high selectivity ($\geqslant$76%) in the entire reaction course and high yield ($\geqslant$75%) to crotyl alcohol. They also display excellent separation and recycling characteristics. A perimeter interface mechanism involving the hydroxyl groups on magnetite and the positively charged gold atoms linked to the lattice oxygen of magnetite is established to address the remarkably high selectivity over the flowerlike Au/Fe_3O_4 catalysts.

1. Introduction

α,β-Unsaturated alcohols, such as allyl alcohol, crotyl alcohol (CROL), and cinnamyl alcohol, represent valuable and versatile intermediates, which occupy an important position in the synthesis of fine chemicals, pharmaceuticals, flavors, fragrances, and herbicides [1]. Currently, good selectivities can be achieved by several means in the hydrogenation of α,β-unsaturated carbonyl compounds. Using $LiAlH_4$ or $NaBH_4$ as the stoichiometric reductant, the conjugated aldehydes can be easily reduced to the corresponding unsaturated alcoholic compounds [2]. Organometallic complex catalysts have been applied in the chemoselective hydrogenation of the C=O bond against the C=C bond [3]. Chemoselective reduction of α,β-unsaturated aldehydes under hydrogen transfer condition with for example isopropanol as the reducing agent, known as the Merwein–Pondorf–Verley reduction, has received much attention in recent years [4]. However, these methods suffer from high costs of the reductants or the organometallic complexes, or difficulties in separating the homogeneous catalysts from the products. It is highly desirable if one can employ the inexpensive dihydrogen and the easily recoverable and highly selective catalyst to transform α,β-unsaturated aldehydes to unsaturated alcohols. But it is unfortunate that the hydrogenation of the C=C bond in α,β-unsaturated aldehydes thermodynamically prevails over the C=O bond, and the C=C bond is also kinetically more active than the C=O bond over most heterogeneous catalysts.

More than two decades ago, Hutchings et al. and Haruta et al. independently verified that gold is an excellent catalyst for low-temperature oxidation of CO and hydrochlorination of acetylene, as acknowledged in Ref. [5]. With the subversion of the traditional impression that gold is catalytically inert, considerable attention has been paid to various heterogeneous hydrogenation reactions catalyzed by oxide-supported gold catalysts, with the chemoselective hydrogenation of α,β-unsaturated aldehydes being one of the most vibrant branches. Since Bailie and Hutchings firstly studied the hydrogenation of α,β-unsaturated aldehyde (in their case crotonaldehyde, CRAL) over gold catalysts [6], most studies have been conducted in gas phase [6–9]. However, it is difficult to achieve high selectivity at high conversion (>95%) through gas phase catalytic reactions. On the contrary, the liquid phase reactions are more advantageous to the yield of the desired product and more appropriate to evaluate the catalysts for industrial applications [10]. For chemoselective hydrogenation of CRAL over oxide-supported gold catalysts, the research has been gradually shifted to liquid phase [11–13]. Among those studies, many experimental results have indicated that reducible oxides are in favor of high activity and selectivity, which is an important reason for the present work to employ magnetite (Fe_3O_4) as the supporting material for gold.

---

* Corresponding authors. Fax: +86 21 65641740.
E-mail addresses: peiyan@fudan.edu.cn (Y. Pei), mhqiao@fudan.edu.cn (M. Qiao).

0021-9517/$ - see front matter © 2011 Elsevier Inc. All rights reserved.
doi:10.1016/j.jcat.2011.04.007

Magnetite has exhibited its prospect in a variety of biological applications such as magnetic carriers for therapeutic agent storage and targeted delivery, magnetic resonance imaging contrast agents, and bioseparation for DNA and proteins [14], to name a few. More interestingly, when magnetite is combined with gold, the Au–Fe_3O_4 heterostructured nanocomposites can further enhance and broaden its potential for biomedical applications [15]. However, there is a surprising dearth of using magnetite as the support for gold in heterogeneous catalysis [16].

Herein, we prepared magnetite-supported gold catalysts by loading gold onto hematite (α-Fe_2O_3) with flowerlike or particulate morphology through homogeneous deposition–precipitation method (HDP), followed by an integrative transformation of the as-prepared hematite-supported Au(III) precursors to Au/Fe_3O_4 at appropriate temperature under reducing atmosphere. The detailed meanings of the names of the samples appeared in this paper were provided in Section 2. On one hand, we attempted to reveal the impact of the morphology of magnetite on the microstructure of the AuNPs. On the other hand, correlations of the structural peculiarities and electronic characters of magnetite and the AuNPs with the activity and selectivity in liquid phase hydrogenation of CRAL to CROL were addressed based on detailed characterization and catalytic results. Magnetic properties of the Au/Fe_3O_4 catalysts arising from magnetite were found to be effective in facilitating the separation and recycling of the catalysts with exceptionally high selectivity to CROL.

2. Experimental

2.1. Catalyst preparation

All reagents were analytical grade (Sinopharm Chemical Reagent) and used as received. Two flowerlike hematite materials were synthesized by an ethylene glycol (EG)-mediated self-assembly process [17]. In one synthesis, $FeCl_3 \cdot 6H_2O$ (1.2 g), urea (2.7 g), and tetrabutylammonium bromide (TBAB, 7.2 g) were added into EG (180 ml) in a 250-ml three-necked flask. The solution was magnetically stirred and heated gradually to the refluxing temperature (ca. 468 K). About 15 min later, a yellow precipitate emerged and rapidly turned to yellowish green. After being stirred for another 8 min, the precipitate turned to totally green. After being refluxed for 30 min, the mixture was cooled down to room temperature naturally. The green precipitate was centrifuged, rinsed with anhydrous ethanol four times, air-dried at 373 K for 12 h, and calcined at 723 K for 3 h in static air to harvest the reddish brown flowerlike hematite. In another synthesis, using $Fe(NO_3)_3$ as the iron source, we also obtained the reddish brown flowerlike hematite through the same route. Identical phenomena during the synthesis were observed. The as-prepared flowerlike hematite materials were designated Fe_2O_3—Cl-*f* and Fe_2O_3—NO_3-*f*, where Cl and NO_3 denote the origin of the iron salts, and *f* denotes their flowerlike morphology.

Two particulate hematite materials, as reference supporting materials, were synthesized via ferric salt precipitation by base, NH_4OH or Na_2CO_3, in an aqueous solution. In one synthesis, $FeCl_3 \cdot 6H_2O$ (2.98 g) was dissolved in 60 ml of water, followed by the addition of NH_4OH solution (20 ml, 25–28 wt.%) dropwisely. After being stirred for 1 h at room temperature, the precipitate was collected by centrifugation and washed repeatedly with deionized (DI) water until neutrality and dried overnight in air at 373 K before being calcined at 623 K for 3 h in static air. In another synthesis, $Fe(NO_3)_3 \cdot 9H_2O$ (4.04 g) was dissolved in 10 ml of water, and the solution was added dropwisely into a Na_2CO_3 solution (10.6 g in 100 ml water). The mixture was stirred vigorously at 353 K for 1 h. The precipitate was aged in the mother liquor at room temperature overnight and treated in a way similar to that of the $FeCl_3$-derived particulate hematite. The as-prepared particulate hematite materials were designated Fe_2O_3—Cl-*p* and Fe_2O_3—NO_3-*p*, where *p* denotes their particulate morphology.

Gold precursor was deposited onto the as-synthesized hematite materials by the HDP method using urea as the precipitant [18]. In a typical preparation, hematite (0.90 g) and urea (1.44 g) were added to a $HAuCl_4$ aqueous solution (57.2 ml, 4.2×10^{-3} M) at room temperature. The suspension was stirred mildly at 353 K for 8 h, during which the pH value gradually increased from 3 to 7. The resulting slurry was gathered by centrifugation and washed with DI water until free of chloride ions ($AgNO_3$ test). The catalyst precursor was air-dried at 353 K for 16 h before being reduced in a tube furnace under 5% H_2/Ar at a flow rate of 50 ml min^{-1}. The reduction temperature was typically increased from 293 to 623 K at a ramping rate of 2 K min^{-1} and held for 3 h, unless otherwise specified. The color of the catalysts turned from reddish brown to black, signifying the phase transformation from hematite to magnetite. Here, the Au(III)/α-Fe_2O_3 catalyst precursors were designated Au(III)/Fe_2O_3—Cl-*f*, Au(III)/Fe_2O_3—NO_3-*f*, Au(III)/Fe_2O_3—Cl-*p*, and Au(III)/Fe_2O_3—NO_3-*p* and the reduced Au/Fe_3O_4 catalysts were designated Au/Fe_3O_4—Cl-*f*-623, Au/Fe_3O_4—NO_3-*f*-623, Au/Fe_3O_4—Cl-*p*-623, and Au/Fe_3O_4—NO_3-*p*-623, where 623 denotes the reduction temperature. The gold loadings on these Au/Fe_3O_4 catalysts were 5.0 ± 0.8 wt.% as determined by inductively coupled plasma atomic emission spectroscopy (ICP-AES, Thermo Elemental IRIS Intrepid II XSP).

2.2. Characterization techniques

Powder X-ray diffraction (XRD) patterns were acquired on a Bruker AXS D8 Advance X-ray diffractometer using nickel filtered Cu Kα radiation (λ = 1.5418 Å). The tube voltage was 40 kV, and the current was 40 mA.

Scanning electron microscopy (SEM) images were recorded on a Philips XL30 electron microscope. The accelerating voltage was in a range of 20–30 kV. The samples were attached to a double-sided carbon conductive adhesive tape on an aluminum slab and coated with gold.

The multi-point Brunauer–Emmett–Teller (BET) surface areas of the hematite materials and Au/Fe_3O_4 catalysts were measured by N_2 physisorption at 77 K on a Micromeritics TriStar3000 apparatus. Before measurements, the samples were degassed at 423 K for 2 h.

Transmission electron microscopy (TEM) experiments were conducted on a JEOL JEM2011 microscope operated at 200 kV. The catalysts were ground in an agate mortar, sonicated in anhydrous ethanol for 10 min, dropped onto a carbon film-coated copper grid, and dried in air. At least 300 particles were measured for particle size determination.

Temperature-programmed reduction of H_2 (H_2-TPR) was performed on a home-made apparatus. About 10 mg of the dried sample (hematite or Au(III)/α-Fe_2O_3 precursor) was loaded in a U-shape quartz tube and purged with high-purity Ar at room temperature for 1 h. Then, the atmosphere was switched to 5% H_2/Ar with a flow rate of 50 ml min^{-1}, and the sample was heated from 300 to 900 K at a heating rate of 10 K min^{-1}.

X-ray photoelectron spectroscopy (XPS) analyses were conducted on a Perkin Elmer PHI5000C instrument using Al Kα radiation as the excitation source ($h\nu$ = 1486.6 eV). The catalyst was mounted on the sample holder, evacuated in the pretreatment chamber at room temperature for 30 min before being transferred to the analyzing chamber, where the background pressure was better than 2×10^{-9} Torr. All the binding energy (BE) values were calibrated by the C 1s peak of contaminant carbon at 284.6 eV.

Magnetic properties of the Au/Fe_3O_4 catalysts were measured on a Standard 7500 Series Lakeshore vibrating sample magnetometer (VSM). Hysteresis loops were recorded at room temperature with the magnetic field sweeping from −9000 to +9000 Oe. The saturation magnetization (M_s), remanent magnetization (M_r), and coercivity (H_c) were derived from the loops of each catalyst.

Extended X-ray absorption fine structure (EXAFS) data of the Au L_{III}-edges (11,919 eV) were collected in the fluorescence mode on the BL14W1 beamline of the Shanghai Synchrotron Radiation Facility (SSRF). The typical electron beam energy was 3.5 GeV, and the current was 300 mA. A cryogenically cooled double-crystal Si(1 1 1) monochromator was used to minimize the harmonics. The catalyst was pressed into an aluminum window with a thickness of ~1 mm, sealed with the Scotch tape, and inserted in the sample stage. The EXAFS spectra were analyzed by the NSRLXAFS 3.0 package according to standard procedures [19]. The experimental backscattering amplitude and phase shift for the Au—Au pair were extracted from the Au foil, and the theoretical parameters for the Au—O and Au—Fe pairs were calculated using the FEFF8.20 code [20] with Au_2O_3 and $Au_{0.05}Fe_{0.95}$ as reference compounds.

2.3. Catalytic testing

Liquid phase hydrogenation of CRAL was conducted in a 100-ml quartz-lined stainless steel autoclave. For each catalytic run, a mixture of CRAL (0.20 ml, 2.42 mmol) and n-C_6H_{14} solvent (20 ml) was charged into the autoclave together with the catalyst (0.4 g, 160–200 mesh). The autoclave was sealed and purged with H_2 for six times. After the desired temperature, 393 K, was reached, the H_2 pressure was raised to 2.0 MPa, and the stirring (1000 rpm) was commenced, which was taken as the beginning of the reaction. The reaction course was monitored by sampling the aliquots at appropriate intervals until the completion of the reaction. The product composition was analyzed by a gas chromatograph (GC Trace Ultra) equipped with an XE-60 capillary column (30 m × 0.32 mm × 0.5 μm) and a flame ionization detector (FID). The products were qualified by comparison with authentic pure reagents (Alfa-Aesar) as well as by gas chromatography–mass spectrometry (GC–MS, Finnigan Voyager). Catalytic activity, expressed as numbers of micromoles of converted substrate per gram of gold per second, was determined from of the initial reaction rate by extrapolating the slope of the concentration–time curves of CRAL to zero reaction time. Selectivity was calculated by $S_i = n_i/\Sigma n_i$, where n_i is the molar percentage of CROL, butanal (BUAL), or butanol (BUOL).

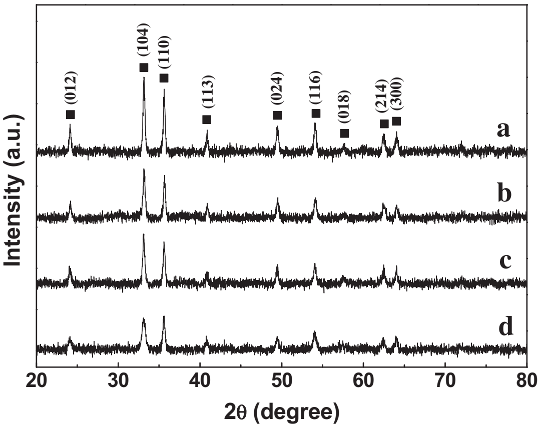

Fig. 1. XRD patterns of (a) Fe_2O_3—Cl-*f*, (b) Fe_2O_3—NO_3-*f*, (c) Fe_2O_3—Cl-*p*, and (d) Fe_2O_3—NO_3-*p*. (■) Hematite (JCPDS 33-0664).

3. Results and discussion

3.1. Physical properties of hematite materials

Fig. 1 shows that the as-synthesized hematite materials possess only characteristic diffraction peaks of hematite (JCPDS 33-0664). The crystallite size is ranged from 17 to 32 nm estimated by the Debye–Scherrer equation (Table 1), and the average crystallite sizes of the hematite materials synthesized by the EG-mediated self-assembly route are larger than those prepared by the base-precipitation route.

Fig. 2a shows the SEM image of the Fe_2O_3—Cl-*f* sample, in which uniform flowerlike architectures of approximately 2 μm in diameter were identified, which is consistent with the observation by Zhong et al. [17]. Inset in Fig. 2a unveils that the petals constituting the flowers are flake-like. When $Fe(NO_3)_3$ was used as the iron source, although the hematite still retains the flowerlike morphology with shrunk dimension (Fig. 2b), inset in Fig. 2b reveals that the petals are rod-like. For comparison, both Fe_2O_3—Cl-*p* and Fe_2O_3—NO_3-*p* samples display the morphology of irregularly packed particulates (Fig. 2c and d).

N_2 physisorption isotherms and Barret–Joyner–Halenda pore size distribution (PSD) curves of the hematite materials are plotted in Fig. S1. These isotherms can be classified as type IV with an H3 hysteresis loop as defined by IUPAC, which is associated with capillary condensation taking place in mesopores and limiting uptake over a range of high relative pressures. The PSDs of both flowerlike hematite materials are weak and broad, while the particulate hematite materials possess relatively sharp mesoporous ordering and narrow PSDs, which explain the higher BET surface areas of the latter (Table 1).

3.2. Redox behaviors of hematite materials and Au(III)/hematite precursors

The reducibility of the hematite materials and the Au(III)/α-Fe_2O_3 precursors was investigated by H_2-TPR, with particular attention on the transformation temperatures of hematite to magnetite in the absence or presence of gold and of gold on supports with different morphologies, since it is known that the transformation temperature of magnetite to wüstite (FeO) and metallic iron is

Table 1
Physicochemical properties of Au/Fe_3O_4 catalysts.

Catalyst	$d_{\alpha\text{-Fe2O3}}$[a] (nm)	d_{Fe3O4}[a] (nm)	S_{BET}, α-Fe_2O_3 ($m^2\ g^{-1}$)	S_{BET}, Au/Fe_3O_4 ($m^2\ g^{-1}$)	H_2:α-Fe_2O_3[b] (molar ratio)	d_{Au}[c] (nm)
Au/Fe_3O_4—Cl-*f*-623	32	27	14	18	0.33/0.33	2.6 ± 0.6
Au/Fe_3O_4—NO_3-*f*-623	32	25	21	16	0.33/0.32	2.7 ± 0.8
Au/Fe_3O_4—Cl-*p*-623	28	30	40	19	0.35/0.33	3.8 ± 1.9
Au/Fe_3O_4—NO_3-*p*-623	17	37	48	15	0.32/0.29	3.5 ± 1.6

[a] The (1 0 4) and (3 1 1) peaks at 33.2° and 35.4° were chosen to calculate the crystallite size of hematite and magnetite in the hematite materials and the Au/Fe_3O_4 catalysts by the Debye–Scherrer equation, respectively.

[b] Calculated from the area of the reduction peak of hematite to magnetite of the hematite materials (left) and the Au(III)/α-Fe_2O_3 precursors (right).

[c] Measured by TEM.

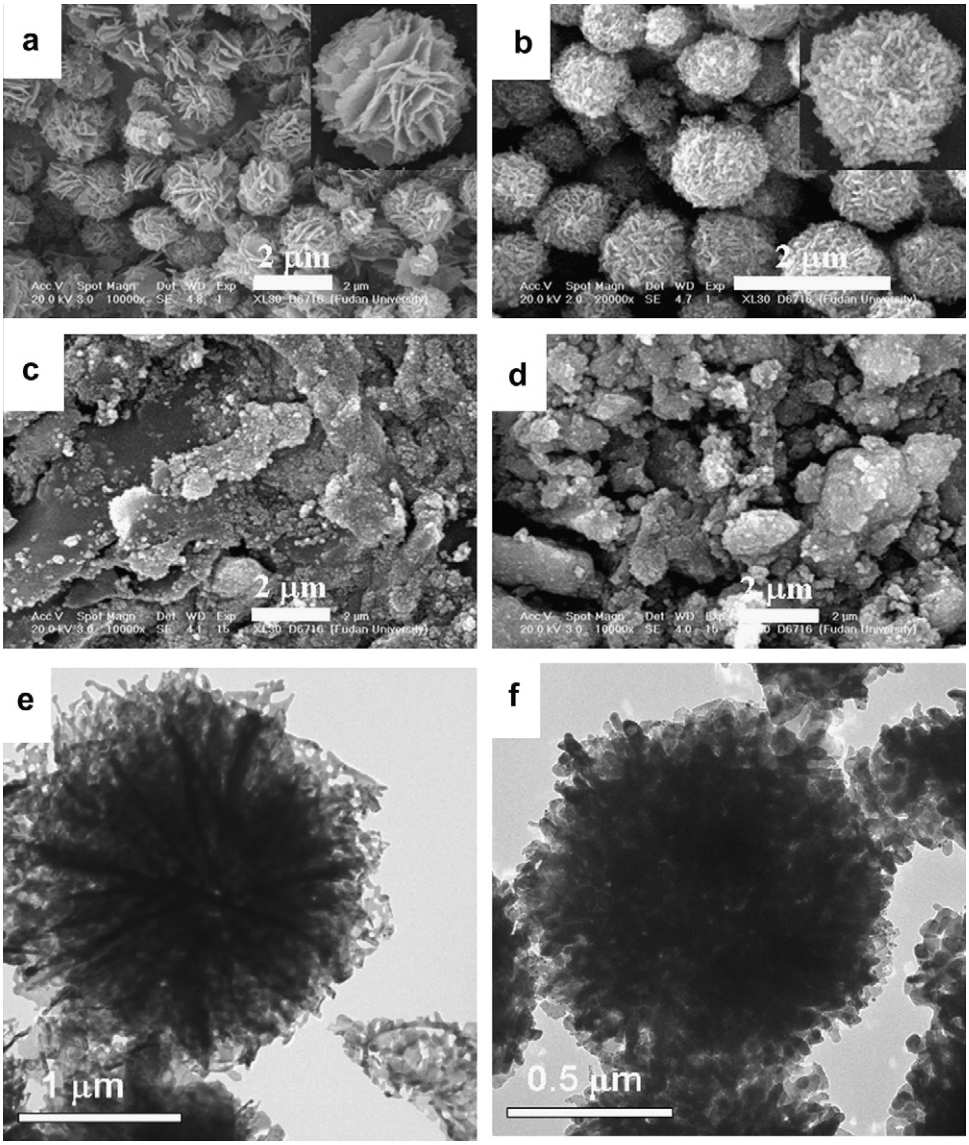

Fig. 2. SEM images of (a) Fe_2O_3—Cl-*f*, (b) Fe_2O_3—NO_3-*f*, (c) Fe_2O_3—Cl-*p*, and (d) Fe_2O_3—NO_3-*p*; and TEM images of (e) Au/Fe_3O_4—Cl-*f*-623, and (f) Au/Fe_3O_4—NO_3-*f*-623. Insets in (a) and (b) are SEM images of an individual Fe_2O_3—Cl-*f* and Fe_2O_3—NO_3-*f* microsphere, respectively.

insensitive to the loading of gold, pretreatment temperature, and surface area [21,22].

Fig. 3 shows that the four hematite materials all display two H_2 consumption peaks. The one at low temperature is ascribed to the reduction from hematite to magnetite, while the one at high temperature to the reduction from magnetite to wüstite and metallic iron [21]. Except for the Fe_2O_3—NO_3-*p* sample that was reduced at ca. 40 K higher (Fig. 3d), the reduction of other three hematite materials was initiated at ca. 530 K and maximized at ca. 660 K. While Munteanu et al. [21] attributed the peak centered at about 660 K to the reduction of hematite to magnetite, the same phase transformation was reported by Milone et al. at 706 K [23]. In addition, it seems that the reduction temperature of hematite to magnetite is not always inversely proportional to the surface area of hematite [22].

Fig. 4 displays the H_2-TPR profiles of the Au(III)/α-Fe_2O_3 precursors. From low to high temperatures, there are three stages assignable to the reduction of Au(III) to Au(0), hematite to magnetite, and magnetite to wüstite and metallic iron [21]. It is notable that the reduction temperatures of Au(III) to Au(0) on both flowerlike hematite materials (Fig. 4a and b) are ca. 20 K higher than those on particulate ones (Fig. 4c and d), implying that the Au(III) species interact more strongly with the flowerlike hematite materials. A tiny shoulder peak at 394 K on the Au(III)/Fe_2O_3—NO_3-*p* precursor (Fig. 4d) was discerned, which is assigned to the stepwise reduction of Au(III) to Au(I) before its final transformation to Au(0) [24], whereas the same reduction behavior was not observed on other three precursors. A comparison with Fig. 3 reveals that upon the deposition of gold, the reduction of hematite to magnetite is shifted to markedly lower temperature, which may be due to the weakening of the Fe—O bonds adjacent to the gold atoms, resulting in higher mobility of lattice oxygen, a well-documented phenomenon for Au/α-Fe_2O_3 catalysts [24]. Alternatively, once the AuNPs are formed, hydrogen spillover over a long distance is invoked concomitantly, which facilitates the reduction in the support. Boccuzzi et al. studied the adsorption of dihydrogen on the Au/α-Fe_2O_3 catalyst by FTIR and found that dihydrogen can be dissociated at room temperature, producing hydrogen atoms that spillover to hematite, where the reduction to magnetite was promoted [25]. In addition, irrespective of the presence of gold or not, the specific amounts

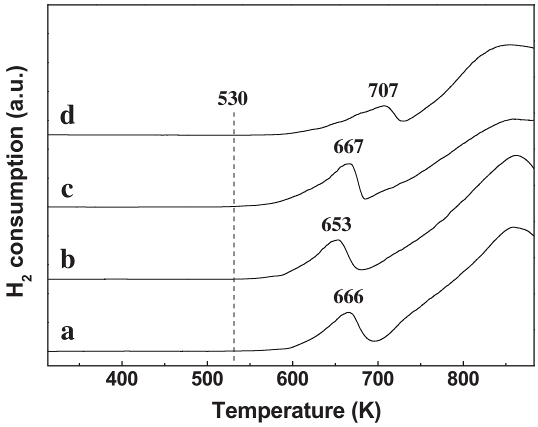

Fig. 3. H_2-TPR profiles of (a) Fe_2O_3—Cl-*f*, (b) Fe_2O_3—NO_3-*f*, (c) Fe_2O_3—Cl-*p*, and (d) Fe_2O_3—NO_3-*p*.

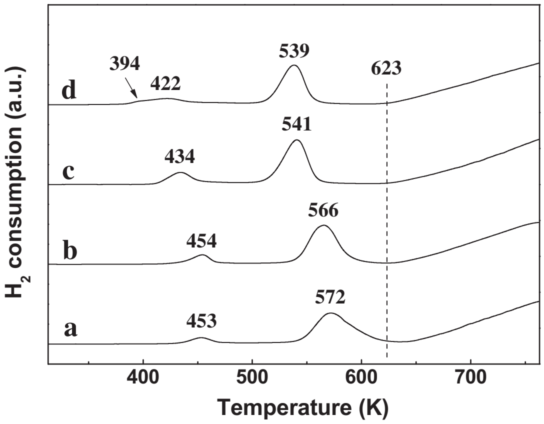

Fig. 4. H_2-TPR profiles of (a) Au(III)/Fe_2O_3—Cl-*f*, (b) Au(III)/Fe_2O_3—NO_3-*f*, (c) Au(III)/Fe_2O_3—Cl-*p*, and (d) Au(III)/Fe_2O_3—NO_3-*p*.

of H_2 consumption from hematite to magnetite remain similar (Table 1).

3.3. Morphology and phase composition of Au/Fe_3O_4 catalysts

Low-magnification TEM images of a single Au/Fe_3O_4—Cl-*f*-623 and Au/Fe_3O_4—NO_3-*f*-623 microsphere are shown in Fig. 2e and f, respectively. It appears that the flowerlike morphology of hematite is nicely carried over to the catalysts. Fig. 2e displays flake-like petals growing outwards from the center of the structure, while Fig. 2f displays columnar rods extending out just like the branch of the frogspawn coral. The center of both microspheres is darker than their exterior, indicating the existence of a thick interior. From the contrast of these TEM images, it also can be judged that there is abundant space between the petals, which would render a good accessibility of the active sites to the reactants.

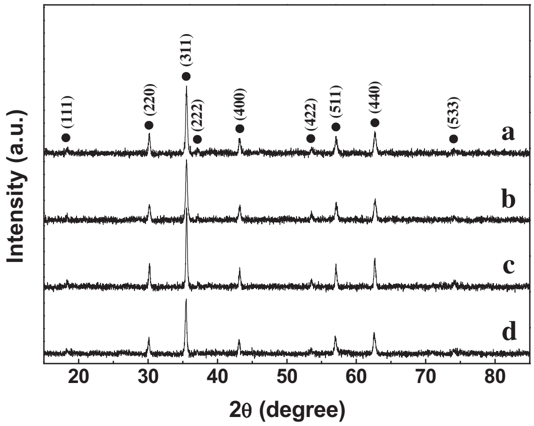

Fig. 5. XRD patterns of (a) Au/Fe_3O_4—Cl-*f*-623, (b) Au/Fe_3O_4—NO_3-*f*-623, (c) Au/Fe_3O_4—Cl-*p*-623, and (d) Au/Fe_3O_4—NO_3-*p*-623. (●) Magnetite (JCPDS 19-0629).

Fig. 5 shows XRD patterns of the Au/Fe_3O_4 catalysts. As proven by H_2-TPR, it is crucial to reduce the Au(III)/α-Fe_2O_3 precursors at an appropriate temperature (623 K) so as to transform hematite thoroughly to magnetite (see Fig. 4) while avoiding over-reduction to wüstite or metallic iron. In this way, the diffraction peaks of Au/Fe_3O_4 catalysts are in good agreement with the standard diffractograms of magnetite (JCPDS 19-0629). It is worth emphasizing that metallic gold are invisible in the diffractogram, suggesting that the gold crystallites are smaller than 5 nm in these catalysts. Haruta indicated that due to the quantum-size effect, the melting point of gold particles of 2 nm in diameter is lowered to 573 K [26]. Milone et al. reported that thermal treatment in air at 673 K was enough to invoke marked sintering of ultrafine gold particles to catalytically inactive bulk gold on Au/Fe_2O_3 catalyst prepared by the DP method (average particle size of ~39.4 nm by TEM) [27]. In this connection, it is anticipated that the AuNPs interact tightly with magnetite in Au/Fe_3O_4 catalysts.

3.4. Particle size and microstructure of Au/Fe_3O_4 catalysts

TEM images and particle size distribution histograms of Au/Fe_3O_4 catalysts are presented in Fig. 6. The Au/Fe_3O_4 catalysts derived from flowerlike hematite materials exhibit narrow particle size distribution of the AuNPs centered at 2.6 and 2.7 nm for Au/Fe_3O_4—Cl-*f*-623 and Au/Fe_3O_4—NO_3-*f*-623 catalysts, respectively (Fig. 6a and b). For comparison, the AuNPs on the Au/Fe_3O_4—Cl-*p*-623 and Au/Fe_3O_4—NO_3-*p*-623 catalysts show particle size distributions centered at 3.8 and 3.5 nm with broad standard deviations of 1.9 and 1.6 nm, respectively (Fig. 6c and d). Some gold particles with diameter larger than 10 nm are randomly distributed on the flat surface of the particulate magnetite materials (marked by white arrows in Fig. 6c and d). Nevertheless, the small particle sizes of the AuNPs observed by TEM justify the absence of diffraction peaks of gold in Fig. 5.

High-resolution transmission electron microscopy (HRTEM) analysis was carried out to investigate the crystallographic relationship between magnetite and the AuNPs on the flowerlike Au/Fe_3O_4 catalysts. In Fig. 6e and f, the AuNPs with basically a rounded shape are uniformly dispersed on the magnetite surface, and no twinned crystallites were observed. Furthermore, HRTEM images clearly show lattice fringes of magnetite growing along the [1 1 1] direction as indicated by the white arrows in Fig. 6e and f. The interplanar spacing is around 4.82 Å, characteristic of the (1 1 1) plane of magnetite. The appearance of this lattice spacing differs from previous work, in which interplanar spacing of 2.52 Å for the (3 1 1) plane was observed on flowerlike magnetite [17]. Such a difference should be attributed to different thermal treatment history between the two magnetite materials. The magnetite materials in our case were obtained by reduction in H_2/Ar atmosphere from the flowerlike hematite, while that of Zhong et al. was obtained from the as-prepared iron oxide precursor by thermal treatment under N_2 atmosphere [17]. On the other hand, the growth of the flake-like petals and columnar rods in flowerlike Au/Fe_3O_4 catalysts along the [1 1 1] direction can be understood by the fact that the (1 1 1) crystallographic plane of cubic magnetite holds the highest surface energy [28].

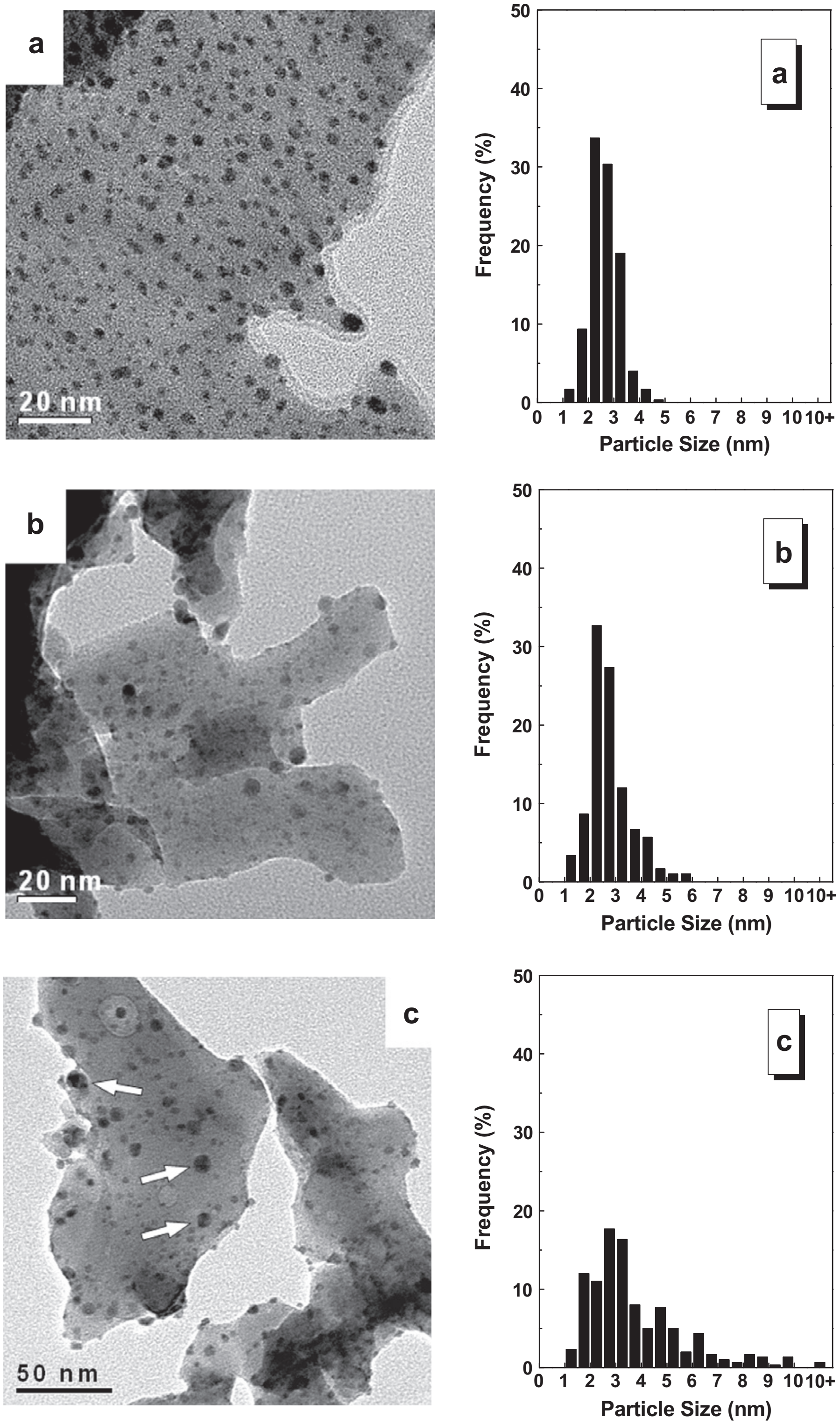

Fig. 6. TEM images and corresponding particle size distribution histograms of the AuNPs for (a) Au/Fe_3O_4—Cl-*f*-623, (b) Au/Fe_3O_4—NO_3-*f*-623, (c) Au/Fe_3O_4—Cl-*p*-623, and (d) Au/Fe_3O_4—NO_3-*p*-623; and HRTEM images of (e) Au/Fe_3O_4—Cl-*f*-623 with FFT, and (f) Au/Fe_3O_4—NO_3-*f*-623 with FFT.

HRTEM images shown in Fig. 6e and f reveal that the lattice spacing of the AuNPs is 2.32 Å, characteristic of the interplanar distance of the (1 1 1) planes of face-centered cubic (*fcc*) gold. The (1 1 1) planes of the AuNPs are parallel to the (1 1 1) planes of magnetite, which is better resolved on the edge of the petals. The parallel crystallographic relationship proves the heteroepitaxial growth of the AuNPs on the underlying magnetite. The digital diffraction patterns inset in Fig. 6e and f indicate again the good alignment of the {1 1 1} reflections of the AuNPs and magnetite, which further confirms the epitaxial relationship. Analogously, Yu et al. [29] prepared dumbbell-like Au—Fe_3O_4 composite nanoparticles through heteroepitaxial growth based on the facilitated matching between the *fcc* lattices of gold (a = 4.08 Å) and magnetite (a = 8.35 Å, close to twice the lattice constant of *fcc* gold). We did

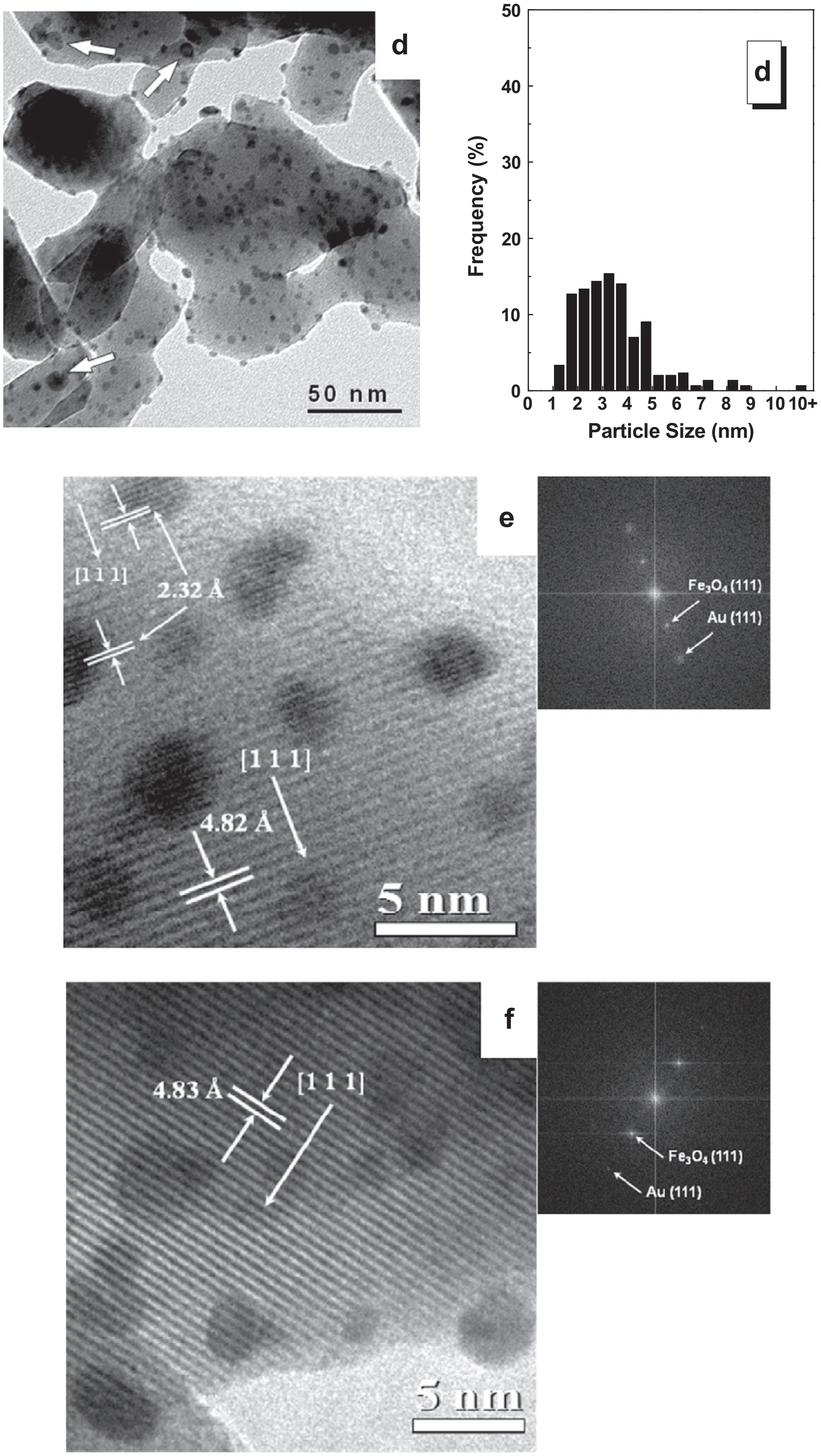

Fig. 6 (*continued*)

not observe the same growth behavior of the AuNPs on two particulate magnetite-supported catalysts.

It is worth noting that although the surface areas of the flowerlike hematite materials are smaller than those of the particulate ones, TEM images show that the dispersion of the AuNPs on flowerlike Au/Fe_3O_4 catalysts is better, suggesting that the AuNPs bind more tightly with the flowerlike magnetite materials. In a separate experiment, we found that when the reduction temperature of the Au(III)/Fe_2O_3—Cl-*f* precursor was elevated from 423 to 773 K, the support was transformed successively from hematite to magnetite/metallic iron hybrid phase (Fig. S2). However, the corresponding average diameter of the AuNPs was only increased from 2.2 to 3.4 nm (Figs. S3 and S4), inferring that epitaxial growth could afford strong stabilizing effect on the AuNPs, resulting in high dispersion and narrow particle size distribution of the AuNPs on flowerlike Au/Fe_3O_4 catalysts.

3.5. Chemical state and surface composition of Au/Fe_3O_4 catalysts

Fig. 7 shows that the Au 4f spectra of Au/Fe_3O_4 catalysts with different morphologies are similar to each other, with the Au $4f_{7/2}$ levels consisting of only one component at ca. 83.7 eV. The negative BE shift of the Au $4f_{7/2}$ level in some case was attributed to electron transfer between materials with different work functions [30]. However, because the work function of magnetite is slightly higher than that of gold [31,32], a slightly positive BE shift of the Au $4f_{7/2}$ level would be expected. The initial state effect arising from quantum-size effects also cannot account for such a BE shift, because it only starts to operate at size below 2 nm [7], while the average sizes of the AuNPs on Au/Fe_3O_4 catalysts exceed that threshold value. On the other hand, considering the spherical shape of the AuNPs as indicated by TEM, one can figure out that the AuNPs with average diameter of 2.6 nm should expose approximately 44.6% of their total atoms on the surface (assuming $D = 1.16/d$, D is the dispersion, and d is the average diameter of the AuNPs) [33]. For the Au/Fe_3O_4—Cl-*p*-623 catalyst with the largest average particle size, a similar approach still gives a surface exposure of as high as 30.5%. Citrin et al. found that for surface gold atoms, their Au $4f_{7/2}$ level shifts to 0.4 eV lower than the bulk value of 84.0 eV and attributed it to the reduced coordination number leading to the narrowing of the valence band due to a combined reduction in *d* band delocalization and *s*–*d* band hybridization [34]. Such a surface atom core level shift may rationalize the lower Au $4f_{7/2}$ BEs observed here.

The Fe 2p spectra shown in Fig. 7 indicate that the Fe $2p_{3/2}$ levels of the four Au/Fe_3O_4 catalysts have identical BE values of magnetite at ca. 710.8 eV [35]. The Fe $2p_{3/2}$ BE of hematite is only 0.4 eV higher than that of magnetite, which may interfere with the assignment of magnetite. However, we do not observe a shake-up secondary structure characteristic of hematite on these spectra, which should otherwise appear at ca. 8.0 eV above the Fe $2p_{3/2}$ peak (indicated by the arrow in Fe 2p spectra) [36]. The intensity of the shake-up structure is originated predominantly from the coupling of the iron core-hole state with the valence band and has turned out to be a highly reliable indicator to distinguish the phase on iron oxide surface [37]. Thus, the surface phase of Au/Fe_3O_4 catalysts is in agreement with their bulk phase.

Table 2 shows that the Au/Fe molar ratios of the two flowerlike Au/Fe_3O_4 catalysts are appreciably higher than those of the particulate Au/Fe_3O_4 catalysts. XPS is a quantitative, surface-sensitive

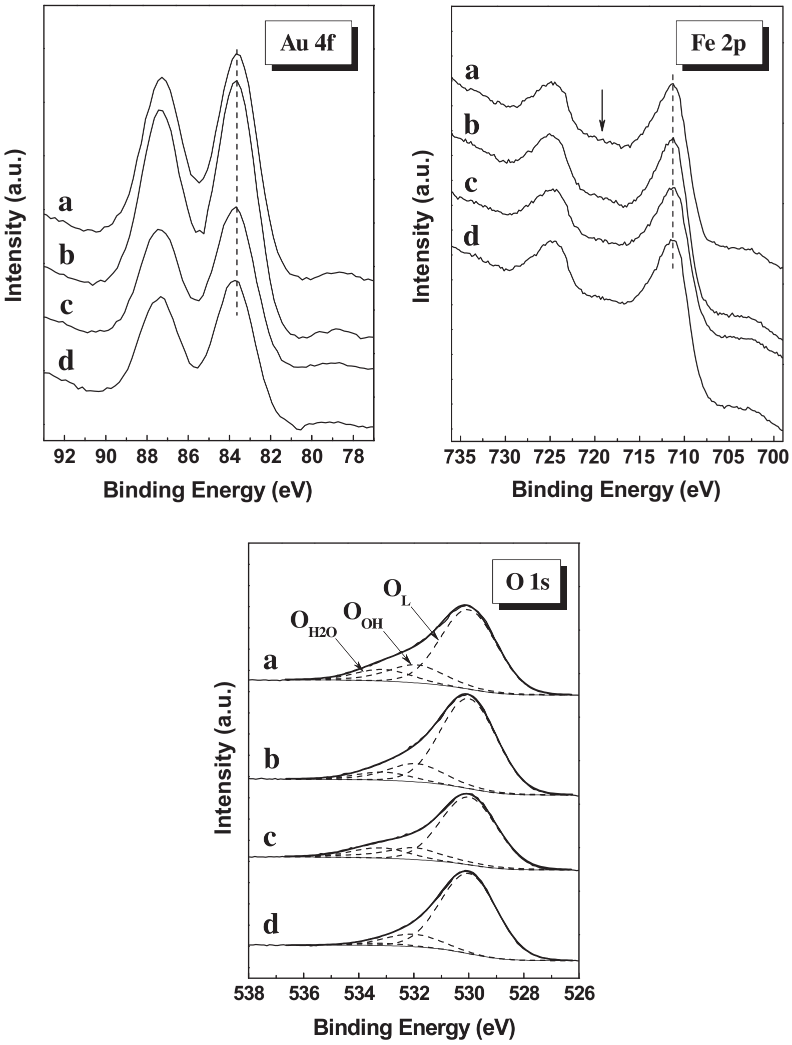

Fig. 7. Au 4f, Fe 2p, and O 1s spectra of (a) Au/Fe_3O_4—Cl-*f*-623, (b) Au/Fe_3O_4—NO_3-*f*-623, (c) Au/Fe_3O_4—Cl-*p*-623, and (d) Au/Fe_3O_4—NO_3-*p*-623.

Table 2
XPS results of Au/Fe_3O_4 catalysts.

Catalyst	Au $4f_{7/2}$ (eV)	Au/Fe (molar ratio)	O_L/Fe[a] (molar ratio)	O_{OH}/Fe[b] (molar ratio)	O_{H2O}/Fe[c] (molar ratio)
Au/Fe_3O_4—Cl-*f*-623	83.6	0.12	2.02	0.55	0.29
Au/Fe_3O_4—NO_3-*f*-623	83.7	0.11	1.99	0.51	0.17
Au/Fe_3O_4—Cl-*p*-623	83.7	0.08	1.68	0.40	0.28
Au/Fe_3O_4—NO_3-*p*-623	83.8	0.06	1.87	0.29	0.05

[a] O_L, surface lattice oxygen.
[b] O_{OH}, surface hydroxyl.
[c] O_{H_2O}, surface water.

analytical tool to the atomic composition of surface layers. At a fixed total volume of the particles, the intensity of the XPS peak depends on the surface-to-bulk atomic ratio of the particles. The larger the surface-to-bulk atomic ratio, the stronger is the XPS peak intensity. Therefore, the higher Au/Fe ratios are a clear indication of the better dispersion of the AuNPs on the flowerlike Au/Fe_3O_4 catalysts than on the particulate catalysts with similar BET surface areas (Table 1), which is consistent with the smaller and more uniform particle sizes of the AuNPs on the flowerlike Au/Fe_3O_4 catalysts.

The O 1s spectra of Au/Fe_3O_4 catalysts are deconvoluted to three components corresponding to lattice oxygen (O_L, O^{2-}) in the oxide at 530.1 eV, oxygen in hydroxyl group (OH) at 531.9 eV, and oxygen in water (H_2O) at 533.1 eV [35]. The O to Fe molar ratios are summarized in Table 2. It is identified that the O_L/Fe molar ratios are higher than the stoichiometry in bulk magnetite, and the deviation is more prominent for the flowerlike catalysts. The surface aggregation of oxygen on iron oxides is not unusual. Sun et al. observed an O_L/Fe molar ratio close to 2 on the surface of an ultrathin FeO(1 1 1) film upon exposure to 50 mbar of O_2 at 450 K [38]. Interestingly, the corresponding low-energy electron diffraction pattern is very similar to that of the pristine FeO(1 1 1)/Pt(1 1 1) surface. The authors speculated that the reconstruction of the Fe and O close-packed layers may be responsible for the O-rich surface, though an exact structure at atomic level is not known. Recently, Rim et al. studied the Fe_3O_4(1 1 1) surface by scanning tunneling microscopy. They proposed that the large O-terminated domains and Fe defects may stabilize the polar Fe_3O_4(1 1 1) surface [39].

3.6. Magnetic properties of Au/Fe_3O_4 catalysts

The Au/Fe_3O_4 catalysts bear excellent ferromagnetic properties sufficient for separation and recycling purposes in liquid phase reaction; their magnetic field-dependent magnetization curves are illustrated in Fig. 8. The corresponding magnetic parameters are summarized in Table 3. For example, for the Au/Fe_3O_4—Cl-*f*-623 catalyst, its M_r is 23.1 emu g^{-1} and H_c is 274 Oe. Upon placement of a magnet near the vial containing the catalyst, the catalyst was readily attracted to the wall within a few seconds, leaving a transparent solution, as visualized in the photograph inserted in Fig. 8a. The M_s of 71.2 emu g^{-1} of the Au/Fe_3O_4—Cl-*f*-623 catalyst is lower than the theoretical value of bulk magnetite (92 emu g^{-1}). A similar decrease in M_s has been observed on magnetite materials with diversified morphologies [40]. Although the exact reason remains elusive, it is generally accepted that the magnetic properties are associated with many factors such as size, morphology, structure, and surface disorder [40]. The lower M_s of our Au/Fe_3O_4 catalysts is probably resulted from the multiple domains and shape anisotropy of the magnetite supports.

3.7. Catalytic performance in liquid phase hydrogenation of CRAL

The time courses of liquid phase hydrogenation of CRAL over the flowerlike and particulate Au/Fe_3O_4 catalysts are plotted in Fig. 9. The products obtained under the present reaction conditions are CROL from C=O hydrogenation, BUAL from C=C hydrogenation, and the completely saturated product, BUOL, which is the consecutive hydrogenation product of either CROL or BUAL, as illustrated in Scheme 1. No other products were identified by GC–MS, which is due to the use of paraffin [12] rather than alcohol as the solvent. Alcohol such as ethanol has been found to react with saturated aldehyde via aldol condensation to acetals [41]. Also, the formation of acetals could be catalyzed by materials with acid sites [12], which are unavailable on magnetite. In addition, we verified in a control experiment that when the feedstock was changed from CRAL to CROL, no tautomerization to BUAL took place under the same reaction conditions.

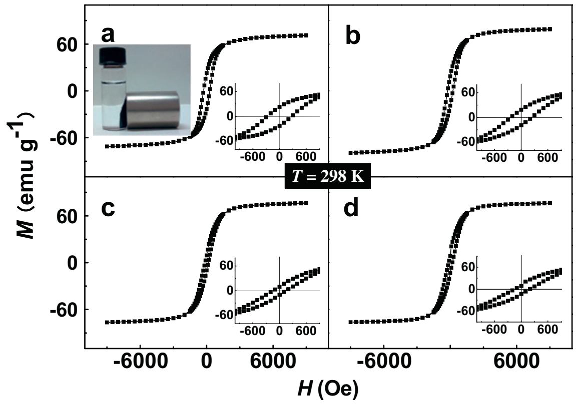

Fig. 8. Room temperature magnetic hysteresis loops of (a) Au/Fe_3O_4—Cl-*f*-623, (b) Au/Fe_3O_4—NO_3-*f*-623, (c) Au/Fe_3O_4—Cl-*p*-623, and (d) Au/Fe_3O_4—NO_3-*p*-623. Inset in (a)–(d): magnified part of their original curve from −1000 to 1000 Oe. Upper left inset: photograph exemplifying the easy separation of Au/Fe_3O_4 catalysts from the products after reaction using a magnet.

Table 3
Magnetic properties of Au/Fe_3O_4 catalysts at 298 K.

Catalyst	M_s (emu g^{-1})	M_r (emu g^{-1})	H_c (Oe)
Au/Fe_3O_4—Cl-*f*-623	71.2	23.1	274
Au/Fe_3O_4—NO_3-*f*-623	79.1	18.7	236
Au/Fe_3O_4—Cl-*p*-623	76.5	9.4	146
Au/Fe_3O_4—NO_3-*p*-623	76.3	8.6	196

The product distributions at the maximum yield of CROL over Au/Fe_3O_4 catalysts are summarized in Table 4. The catalysts reduced at 623 K showed excellent selectivities to CROL (68–78%) even at nearly complete conversion of CRAL (Entries 1, 5, 6, and 7 in Table 4), whereas the flowerlike catalysts additionally displayed much higher initial activity (r_0) than the particulate catalysts by a factor of ca. 2.5. Although it remains open that the active sites for dihydrogen dissociation are located either at low coordinated corner or edge sites of gold particles or at the perimeter around gold particles [42,43], it is believed that the dissociation of dihydrogen is the rate-determining step on gold catalysts [8]. No

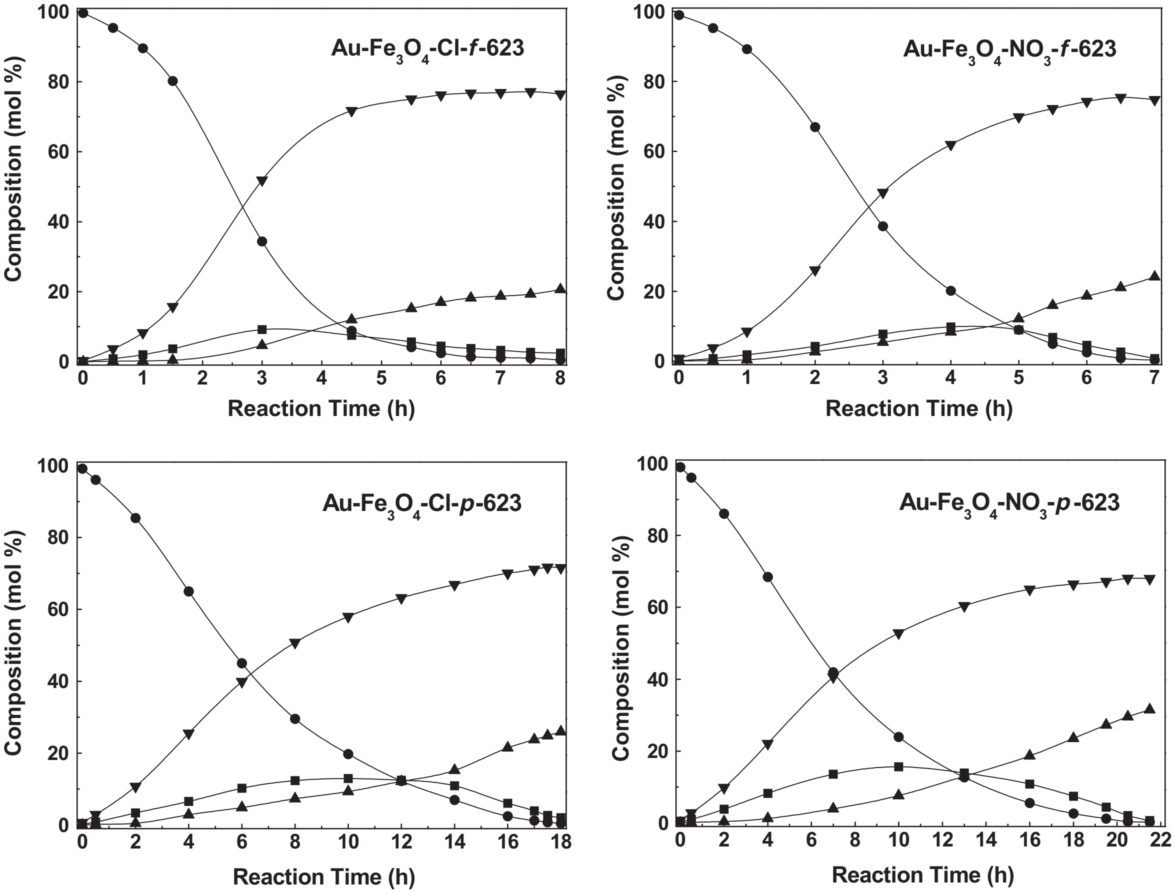

Fig. 9. Time dependences of CRAL hydrogenation over Au/Fe_3O_4 catalysts. Reaction conditions: catalyst (0.4 g), CRAL (2.42 mmol), n-C_6H_{14} (20 ml), H_2 pressure (2 MPa), and temperature (393 K). (▼) CROL, (▲) BUOL, (●) CRAL, and (■) BUAL.

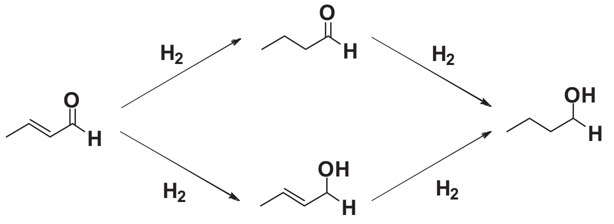

Scheme 1. Reaction pathways of CRAL hydrogenation over Au/Fe_3O_4 catalysts.

matter where the active sites are, the number of active sites is expected to be inversely proportional to the particle size of gold and consequently, the flowerlike Au/Fe_3O_4 catalysts with smaller AuNPs would exhibit higher activity than the particulate catalysts.

We have also investigated the influence of the reduction temperature on the catalytic performance of the flowerlike Au/Fe_3O_4 catalysts. It turns out that the Au/Fe_3O_4—Cl-*f* catalysts reduced at 423, 523, and 773 K (Entries 2, 3, and 4 in Table 4) showed lower selectivities to CROL than that reduced at 623 K, especially for the Au/Fe_3O_4—Cl-*f*-423 catalyst. According to Figs. S2a and 4a,

Table 4
Hydrogenation results of CRAL over Au/Fe_3O_4 catalysts.[a]

Entry	Catalyst	Conv.[b] (%)	Sel.[b] (%)			S_0[c] (%)	Y[b] (%)	t[b] (h)	r_0[d]
			CROL	BUAL	BUOL				
1	Au/Fe_3O_4—Cl-*f*-623	>99	78	3	19	81	77	7.5	5.03
2	Au/Fe_3O_4—Cl-*f*-423	>99	50	4	46	52	50	5.5	22.7
3	Au/Fe_3O_4—Cl-*f*-523	98.6	71	1	28	72	70	4.5	6.87
4	Au/Fe_3O_4—Cl-*f*-773	>99	68	5	27	69	67	10	3.23
5	Au/Fe_3O_4—NO_3-*f*-623	>99	76	2	22	80	75	6.5	4.24
6	Au/Fe_3O_4—Cl-*p*-623	>99	72	3	25	74	72	17.5	1.98
7	Au/Fe_3O_4—NO_3-*p*-623	>99	68	2	30	71	68	20.5	1.56
8	Au/Fe_3O_4—Cl-*f*-623[e]	97.8	76	4	20	–	74	7.5	–
9	Au/Fe_3O_4—NO_3-*f*-623[f]	98.6	73	4	23	–	72	6.5	–

[a] Reaction conditions: catalyst (0.4 g), CRAL (2.42 mmol), n-C_6H_{14} (20 ml), H_2 (2 MPa), and 393 K.

[b] Values corresponding to the maximum yield of CROL.

[c] Initial selectivity to CROL obtained by extrapolating the slope of the selectivity–time curve of CROL to zero reaction time.

[d] Unit in $\mu mol/g_{Au}^{-1}\ s^{-1}$.

[e] Results at the sixth run.

[f] Results at the third run.

the temperature of 423 K is not high enough to transform hematite to magnetite even in the presence of gold. Lenz et al. have found that irrespective of the preparation method, HDP or direct anionic exchange (DAE), the selectivity to CROL over Au/α-Fe_2O_3 catalysts ranges within 45–48% [11], similar to the result over the Au/Fe_3O_4—Cl-*f*-423 catalyst, although the sizes of the AuNPs in their catalysts are different from ours (7.7 nm for HDP and 5.7 nm for DAE vs. 2.2 nm in our case), indicating the important role of the support on the selectivity. Once the reduction temperature was elevated to 523 K, hematite was completely transformed to magnetite (Fig. S2b), and concomitantly the selectivity to CROL was dramatically increased from 50% to 71%. Even though the reduction temperature was raised to as high as 773 K, at which a small portion of metallic iron emerged (Fig. S2c), the selectivity to CROL still maintained at a high level (66%). These results unambiguously confirm the essential role of magnetite in enhancing the selectivity to CROL on gold catalysts.

The recycling properties of two flowerlike Au/Fe_3O_4 catalysts reduced at 623 K were studied in detail, since they exhibited the best activity and selectivity. It should be mentioned that due to their ferromagnetic properties, these catalysts aggregated after magnetic separation. But they were redispersible in the reaction solution simply by stirring. After each catalytic run, the catalysts were separated from the reaction solution by a magnet, washed with *n*-C_6H_{14} and sonicated for four times, and reused in a successive run without reactivation. In Fig. 10, it is shown that the conversion of CRAL over the Au/Fe_3O_4—NO_3-*f*-623 catalyst declined from 99% to 87% at the fifth run, while the Au/Fe_3O_4—Cl-*f*-623 catalyst is more stable and could be used for six runs without deactivation. The selectivities to CROL decreased slightly to 76% at the sixth run over the Au/Fe_3O_4—Cl-*f*-623 catalyst and to 73% at the third run over the Au/Fe_3O_4—NO_3-*f*-623 catalyst (Entries 8 and 9 in Table 4). The TEM images of the Au/Fe_3O_4—Cl-*f*-623 and Au/Fe_3O_4—NO_3-*f*-623 catalysts after eight and five runs, respectively, show inappreciable increase in the average particle size of gold, except that the AuNPs became more round and a few large particles appeared due to the coalescence or Ostwald ripening during repetitive catalytic runs (Fig. S5) [44]. To better understand the reason for catalyst deactivation, a systematic study is required, which is being planned in these laboratories.

3.8. Mechanism of CRAL hydrogenation on Au/Fe_3O_4 catalysts

In Table S1, we compared the selectivity to CROL over the Au/Fe_3O_4—Cl-*f*-623 catalyst with those over literature oxide-supported gold catalysts for the same reaction. One cannot make too much of the differences, because no suitable correction can be made for the reaction conditions. However, it is apparent that gold supported on magnetite is more selective than other oxide-supported gold catalysts (Table S1). In addition, the effect of the so-called "active" or "inert" supports seems not operative in the case of CRAL hydrogenation.

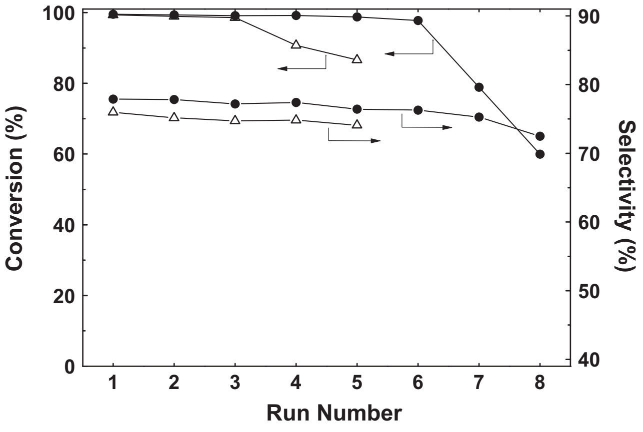

Fig. 10. CRAL hydrogenation over Au/Fe_3O_4—Cl-*f*-623 (●) and Au/Fe_3O_4—NO_3-*f*-623 (▲) for successive runs. Conversion and selectivity in each run were determined after 7.5 and 6.5 h of reaction for Au/Fe_3O_4—Cl-*f*-623 and Au/Fe_3O_4—NO_3-*f*-623, respectively. The reaction conditions are given in Fig. 9.

Since the leading work of Bailie and Hutchings on CRAL hydrogenation over Au-oxide catalyst [6], there is no consensus on the nature of the active sites on which α,β-unsaturated alcohol is formed. Particle size [6,7,9], geometric configuration [11], and electron density [7,12,23] of gold, or reducibility [23], surface area [9], and defect sites (oxygen vacancies) [9] of the oxide supports, have been raised as the possible reasons for the selectivity difference. However, as to the size effect, Zanella et al. only observed a 10% variation in the selectivity to CROL when the average diameter of the AuNPs in Au/TiO_2 catalysts was increased from 1.7 to 8.7 nm [8], whereas Claus et al. [7] found a distinct impact of particle size on the formation of α,β-unsaturated alcohols. So, the particle size of gold looks unlikely an exclusive factor in determining the selectivity.

As to the electronic effect, Claus et al. proposed that gold particles anchored on ZrO_2 or TiO_2 with paramagnetic F-centers have an increased electron density due to charge transfer from the support to gold, which could decrease the binding energy of the C=C bond for increased four-electron repulsion but at the same time enhance the back-donating interaction with π^*C=O, thus favoring the hydrogenation of the C=O bond [7]. Analogously, Milone et al. found a correlation between the reducibility of the iron oxides and the activity and selectivity to CROL on iron oxide-supported gold catalysts and argued that active and selective sites are negatively charged gold particles formed through electron transfer from the reduced iron oxide to gold [23]. However, according to the Au 4f and Fe 2p spectra in Fig. 7, charge transfer from magnetite to the AuNPs is negligible in our Au/Fe_3O_4 catalysts, at least at a level discernible by this technique.

Yang et al. studied the adsorption of CRAL on Au(1 1 1) single crystal and on Au_{19} cluster [13]. They found that the adsorption energy of CRAL on bulky Au(1 1 1) single crystal is marginal, while the Au_{19} cluster, specifically its corner sites, is able to accommodate this molecule with either η_2-$\pi_{C=C}$ (−0.48 eV) or η_1-on-top (−0.27 eV) adsorption configuration. It is acknowledged that the relative binding strength of the C=C and C=O bonds in α,β-unsaturated aldehydes to the catalyst surface is crucial for the selectivity [45]. The preferential binding through the C=C bond in the η_2-$\pi_{C=C}$ rather than the η_1-on-top configuration on the Au_{19} cluster, as indicated by the more negative adsorption energy of the former, should favor the formation of BUAL in the hydrogenation of CRAL. So, that work clearly demonstrates that the AuNPs alone are intrinsically not favorable for the hydrogenation of the C=O bond. In this connection, the excellent selectivity on the Au/Fe_3O_4 catalysts cannot be ascribed solely to the geometric and electronic properties of gold itself; rather, the role of the support should also be taken into consideration.

Recently, Wang et al. investigated the hydrogenation pathways of acrolein on a model Au/*m*-ZrO_2 catalyst within the framework of density functional theory (DFT) periodic calculations [46]. They demonstrated that the Au(I) monomer supported at the $ZrO_2(\bar{2}12)$ surface exhibits desirable selectivity to allyl alcohol, and both gold and ZrO_2 surface atoms participate in the hydrogenation steps, which resembles a perimeter interface involving the peripheral atoms of a gold particle and the proximate metal oxide. The idea that the active sites are located at the gold–metal oxide interface has been adopted to interpret the catalytic activity of gold catalysts in CO oxidation. In fact, Milone et al. have noticed the synergetic effect between gold and iron oxide in their Au/Fe_2O_3

catalysts on the activation of the C═O bond in α,β-unsaturated aldehyde or ketone, but with no further elucidation [27]. According to Wang et al., the most preferred pathway for acrolein hydrogenation is the attachment of one hydrogen atom in the hydroxyl group on ZrO_2 to the oxygen end of acrolein to form an intermediate adsorbed on gold, followed by the shifting of another hydrogen atom from Au(I) to α-C to form allyl alcohol. The reaction barrier of this pathway is only 0.46 eV, which is at least 0.36 eV lower than other three pathways considered. Mülliken charge analysis showed that dihydrogen cleavage on the Au—ZrO_2 interface results in two hydrogen atoms with different natures: The one in the form of surface hydroxyl group of ZrO_2 is proton-like, whereas the other on Au(I) is negatively charged and thus hydride-like [46]. These oppositely charged hydrogen species are expected to interact more favorably with the polar C═O bond than with the apolar C═C bond, leading to a superior selectivity to allyl alcohol [46].

The dissociation of dihydrogen on the interface sites of metal oxide-supported gold catalyst has recently been verified experimentally. Fujitani et al. found that the Au(1 1 1), Au(3 1 1), or TiO_2(1 1 0) surface alone cannot invoke H_2—D_2 exchange, but TiO_2/Au(1 1 1) or Au/TiO_2(1 1 0) system can, suggesting that the Au—O—Ti linkage at the interface is essential for the dissociation of dihydrogen [43]. On the other hand, the presence of the positively charged gold atoms at the gold–oxide interface is common for metal oxide-supported gold catalysts. According to the DFT calculations of Au/MO_2 (M = Ti or Ce) systems, the gold atoms bearing a net positive charge are present in the first layer of the cluster due to the formation of the Au—O—M linkage. The positive charge on gold atoms at the interface is +0.30e in Au—O—Ti and $\leqslant$+0.18e in Au—O—Ce linkages [42,47].

In light of the findings discussed above, we brought forward a perimeter interface mechanism based on Wang et al. [46]. This mechanism involves the hydroxyl group on magnetite near the periphery of the AuNPs and gold atoms bonding with magnetite at the borderline for the chemoselective hydrogenation of CRAL to CROL. It has been reported by Boccuzzi et al. that the hydroxyl groups are highly apt to situate at the interface between gold and hematite [25], which may also be held by Au/Fe_3O_4 catalysts. As depicted in Scheme 2, the oxygen end of the C═O bond in the CRAL molecule is firstly attacked by hydrogen atom in the hydroxyl group on magnetite, forming a CH_3—CH═CH—CHOH intermediate, followed by sterically preferred adsorption via α-C on peripheral gold atom, where one dissociated hydrogen atom from heterolytic cleavage of dihydrogen is added to α-C. The other dissociated hydrogen atom replenishes the depleted hydrogen in the hydroxyl group on magnetite, thus completing the catalytic cycle.

The perimeter interface mechanism is substantiated by a linear relationship between the surface O_{OH}/Fe ratio derived from XPS and the S_0, namely, the more abundance the surface hydroxyl groups, the higher the selectivity to CROL (Fig. 11), which validates the idea that the surface hydroxyl group on magnetite participates in the hydrogenation of the C═O bond. On the other hand, although both HRTEM revealing the smaller particle size and epitaxial growth of AuNPs and H_2-TPR revealing the higher reduction temperature of Au(III) imply a stronger interaction of gold particles with flowerlike magnetite materials than with particulate ones, more direct evidence for gold atoms in the form of Au—O—Fe linkage which is indispensable not only to heterolytic cleavage of dihydrogen but also to the energetically favorable adsorption configuration of CRAL.

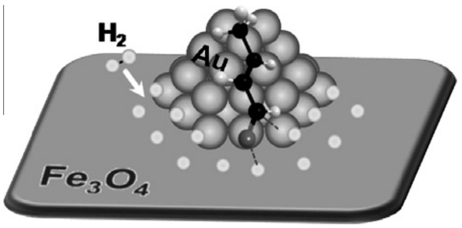

Scheme 2. A diagram of the chemoselective hydrogenation of CRAL to CROL at the perimeter interface of Au/Fe_3O_4 catalysts. O: gray, H: white, and C: black.

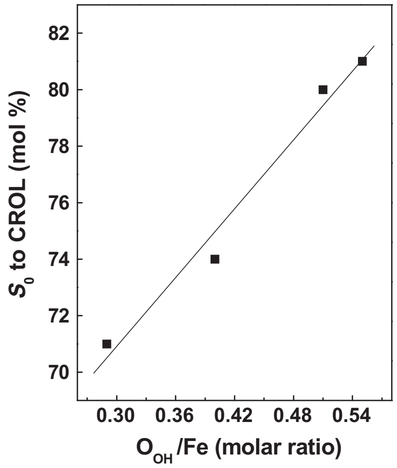

Fig. 11. Correlation between the initial selectivity (S_0) to CROL and surface O_{OH}/Fe molar ratio on Au/Fe_3O_4 catalysts.

Table 5
EXAFS fit parameters for Au/Fe_3O_4—Cl-*f*-623 and Au/Fe_3O_4—Cl-*p*-623 catalysts from first-shell analysis of the Au L_{III}-edges.[a]

Catalyst	Shell	*N*	*R* (Å)	$\Delta\sigma^2$ (10^{-3} Å^2)	ΔE_0 (eV)
Au/Fe_3O_4—Cl-*f*-623	Au—Au	9.1	2.84	8.24	3.84
	Au—O	1.4	1.98	8.10	−10.0
	Au—Fe[b]	0.1	2.72	0.37	−10.0
Au/Fe_3O_4—Cl-*p*-623	Au—Au	9.8	2.85	8.24	7.61
	Au—O	1.0	2.15	8.10	−0.50
	Au—Fe[b]	0.5	2.72	0.37	−7.13

[a] *N*, coordination number; *R*, distance between absorber and backscatterer atoms; $\Delta\sigma^2$, Debye–Waller factor; ΔE_0, inner potential correction. Errors: *N*, ±10%; *R*, ±0.02 Å.

[b] This contribution is too small to allow for a confident assignment. It was included to make the overall fitting complete.

To verify this point, we examined the catalysts by EXAFS, a powerful and specific tool for probing local atomic structure of materials. Fig. S6 shows the Au L_{III}-edge $k^3\chi(k)$ EXAFS data for Au/Fe_3O_4—Cl-*f*-623 and Au/Fe_3O_4—Cl-*p*-623 catalysts as two representatives. The structural parameters are summarized in Table 5. The first coordination shell was fitted; no higher shells were present. The good quality of the fitting is confirmed by the close resemblance of the simulated k_3-weighted normalized EXAFS oscillations to the experimental data. The Au—Au coordination number (*N*) and distance (*R*) were 9.1 and 2.84 Å for Au/Fe_3O_4—Cl-*f*-623, while 9.8 and 2.85 Å for Au/Fe_3O_4—Cl-*p*-623, which corroborates well with the relationship between the Au—Au coordination number and distance summed up by Miller et al. [48]. More intriguingly, a contribution of a light scatterer with *N* of 1.4 and 1.0 for Au/Fe_3O_4—Cl-*f*-623 and Au/Fe_3O_4—Cl-*p*-623, respectively, was observed at ca. 2 Å (Table 5 and Fig. 12), which is ascribable to gold atoms in direct contact with the lattice oxygen of magnetite. The existence of the Au—O coordination at the similar distance in the reduced gold catalysts has been observed on Au/TiO_2 [49] and Au/MgO [50] catalysts. It is conceivable that as the loading of gold on Au/Fe_3O_4—Cl-*f*-623 and Au/Fe_3O_4—Cl-*p*-623 catalysts is identical, the

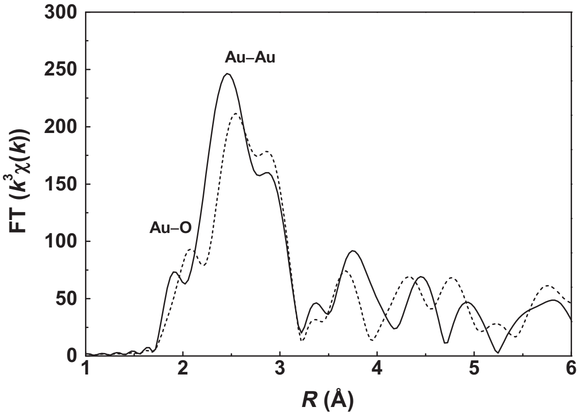

Fig. 12. Au L_{III}-edge k^3-weighted Fourier transforms of Au/Fe_3O_4—Cl-*f*-623 (dashed line) and Au/Fe_3O_4—Cl-*p*-623 (solid line).

smaller the AuNPs, the larger the total number of gold atoms at the perimeter interface. Since the population of the Au—O—Fe linkage on the flowerlike magnetite-supported gold catalyst is higher than that on the particulate magnetite-supported catalyst, it follows that the selectivity to CROL is higher on the former in the framework of the perimeter interface mechanism.

4. Conclusions

Due to the heteroepitaxial growth of gold nanoparticles on flowerlike magnetite, the AuNPs are smaller and more homogeneous in dimension. In liquid phase hydrogenation of CRAL to CROL, the flowerlike magnetite-supported gold catalysts are much more active and slightly more selective than the particulate magnetite-supported catalysts, while both kinds of Au/Fe_3O_4 catalysts being more selective than the literature oxide-supported gold catalysts for the same reaction. Au/Fe_3O_4 catalysts can be magnetically separated from the products for recycling purpose taking advantage of the magnetic property of magnetite. Based on literature work and detailed characterizations, a perimeter interface mechanism involving the hydroxyl group on magnetite near the periphery of the AuNPs and the interfacial Au—O—Fe linkage is proposed to account for the high selectivity to CROL over Au/Fe_3O_4 catalysts. This work shows the prospect of improving the sluggish kinetics of C═O bond hydrogenation in α,β-unsaturated aldehydes or ketones by elaborately tailoring the interface property of the oxide-supported gold catalysts.

Acknowledgments

This work was supported by the Program of New Century Excellent Talents in Universities (NCET-08-0126), the Science & Technology Commission of Shanghai Municipality (08DZ2270500, 09ZR1402300, 10JC1401800), and the NSF of China (21073043, 20803011). And we thank Mr. Z. Shi and Prof. S.M. Zhou of Department of Physics, Fudan University, for the measurement of magnetic properties.

Appendix A. Supplementary material

Supplementary data associated with this article can be found, in the online version, at doi:10.1016/j.jcat.2011.04.007.

References

[1] P. Gallezot, D. Richard, Catal. Rev. Sci. Eng. 40 (1998) 81.
[2] B. Tamami, H. Mahdavi, Tetrahedron 59 (2003) 821.
[3] T. Ohkuma, H. Ooka, T. Ikariya, R. Noyori, J. Am. Chem. Soc. 117 (1995) 10417.
[4] X. Wu, J. Liu, X. Li, A. Zanotti-Gerosa, F. Hancock, D. Vinci, J. Ruan, J. Xiao, Angew. Chem. Int. Ed. 45 (2006) 6718.
[5] A.S.K. Hashmi, G.J. Hutchings, Angew. Chem. Int. Ed. 45 (2006) 7896.
[6] J.E. Bailie, G.J. Hutchings, Chem. Commun. (1999) 2151.
[7] P. Claus, A. Brückner, C. Mohr, H. Hofmeister, J. Am. Chem. Soc. 122 (2000) 11430.
[8] R. Zanella, C. Louis, S. Giorgio, R. Touroude, J. Catal. 223 (2004) 328.
[9] B. Campo, M. Volpe, S. Ivanova, R. Touroude, J. Catal. 242 (2006) 162.
[10] B.C. Campo, M.A. Volpe, C.E. Gigola, Ind. Eng. Chem. Res. 48 (2009) 10234.
[11] J. Lenz, B.C. Campo, M. Alvarez, M.A. Volpe, J. Catal. 267 (2009) 50.
[12] Q.Y. Yang, Y. Zhu, L. Tian, S.H. Xie, Y. Pei, H. Li, H.X. Li, M.H. Qiao, K.N. Fan, Appl. Catal. A 369 (2009) 67.
[13] X. Yang, A. Wang, X. Wang, T. Zhang, K. Han, J. Li, J. Phys. Chem. C 113 (2009) 20918.
[14] J.H. Lee, Y.M. Huh, Y.W. Jun, J.W. Seo, J.T. Jang, H.T. Song, S. Kim, E.J. Cho, H.G. Yoon, J.S. Suh, J. Cheon, Nat. Med. 13 (2007) 95.
[15] C. Xu, J. Xie, D. Ho, C. Wang, N. Kohler, E.G. Walsh, J.R. Morgan, Y.E. Chin, S. Sun, Angew. Chem. Int. Ed. 47 (2008) 173.
[16] H.F. Yin, C. Wang, H.G. Zhu, S.H. Overbury, S.H. Sun, S. Dai, Chem. Commun. (2008) 4357.
[17] L.S. Zhong, J.S. Hu, H.P. Liang, A.M. Cao, W.G. Song, L.J. Wan, Adv. Mater. 18 (2006) 2426.
[18] Q.Y. Yang, Y. Zhu, L. Tian, Y. Pei, M.H. Qiao, K.N. Fan, Acta Phys. Chim. Sin. 25 (2009) 1853.
[19] B. Lengeler, P. Eisenberger, Phys. Rev. B 21 (1980) 4507.
[20] A. Ankudinov, B. Ravel, J.J. Rehr, FEFF8, Version 8.20, University of Washington, Seattle, WA, 2002.
[21] G. Munteanu, L. Ilieva, D. Andreeva, Thermochim. Acta 291 (1997) 171.
[22] G. Neri, A.M. Visco, S. Galvagno, A. Donato, M. Panzalorto, Thermochim. Acta 329 (1999) 39.
[23] C. Milone, R. Ingoglia, L. Schipilliti, C. Crisafulli, G. Neri, S. Galvagno, J. Catal. 236 (2005) 80.
[24] A. Venugopal, M.S. Scurrell, Appl. Catal. A 258 (2004) 241.
[25] F. Boccuzzi, A. Chiorino, M. Manzoli, D. Andreeva, T. Tabakova, J. Catal. 188 (1999) 176.
[26] M. Haruta, CATTECH 6 (2002) 102.
[27] C. Milone, R. Ingoglia, A. Pistone, G. Neri, F. Frusteri, S. Galvagno, J. Catal. 222 (2004) 348.
[28] B. Jia, L. Gao, J. Phys. Chem. C 112 (2008) 666.
[29] H. Yu, M. Chen, P.M. Rice, S.X. Wang, R.L. White, S. Sun, Nano Lett. 5 (2005) 379.
[30] S. Arrii, F. Morfin, A.J. Renouprez, J.L. Rousset, J. Am. Chem. Soc. 126 (2004) 1199.
[31] W. Weiss, W. Ranke, Prog. Surf. Sci. 70 (2002) 1.
[32] D.R. Lide, CRC Handbook of Chemistry and Physics, 89th ed., CRC Press, Boca Raton, 2009. pp. 12–114.
[33] G. Bergeret, P. Gallezot, Particle size and dispersion measurements, in: G. Ertl, H. Knözinger, F. Schüth, J. Weitkamp (Eds.), Handbook of Heterogeneous Catalysis, Wiley-VCH, Weinheim, 2008, p. 738.
[34] P.H. Citrin, G.K. Wertheim, Y. Baer, Phys. Rev. Lett. 41 (1978) 1425.
[35] T. Choudhury, S.O. Saied, J.L. Sullivan, A.M. Abbot, J. Phys. D 22 (1989) 1185.
[36] Th. Schedel-Niedrig, W. Weiss, R. Schlögl, Phys. Rev. B 52 (1995) 17449.
[37] M. Muhler, R. Schlögl, G. Ertl, J. Catal. 138 (1992) 413.
[38] Y.N. Sun, Z.H. Qin, M. Lewandowski, E. Carrasco, M. Sterrer, S. Shaikhutdinov, H.J. Freund, J. Catal. 266 (2009) 359.
[39] K.T. Rim, D. Eom, L. Liu, E. Stolyarova, J.M. Raitano, S.W. Chan, M. Flytzani-Stephanopoulos, G.W. Flynn, J. Phys. Chem. C 113 (2009) 10198.
[40] D.E. Zhang, X.J. Zhang, X.M. Ni, J.M. Song, H.G. Zheng, Cryst. Growth Des. 7 (2007) 2117.
[41] Y. Pei, P.J. Guo, M.H. Qiao, H.X. Li, S.Q. Wei, H.Y. He, K.N. Fan, J. Catal. 248 (2007) 303.
[42] M. Boronat, F. Illas, A. Corma, J. Phys. Chem. A 113 (2009) 3750.
[43] T. Fujitani, I. Nakamura, T. Akita, M. Okumura, M. Haruta, Angew. Chem. Int. Ed. 48 (2009) 9515.
[44] M.T. Bore, H.N. Pham, E.E. Switzer, T.L. Ward, A. Fukuoka, A.K. Datye, J. Phys. Chem. B 109 (2005) 2873.
[45] V. Ponec, Appl. Catal. A 149 (1997) 27.
[46] C.M. Wang, K.N. Fan, Z.P. Liu, J. Catal. 266 (2009) 343.
[47] C. Zhang, A. Michaelides, D.A. King, S.J. Jenkins, J. Am. Chem. Soc. 132 (2010) 2175.
[48] J.T. Miller, A.J. Kropf, Y. Zha, J.R. Regalbuto, L. Delannoy, C. Louis, E. Bus, J.A. van Bokhoven, J. Catal. 240 (2006) 222.
[49] J. Guzman, B.C. Gates, J. Phys. Chem. B 107 (2003) 2242.
[50] J. Guzman, S. Kuba, J.C. Fierro-Gonzalez, B.C. Gates, Catal. Lett. 95 (2004) 77.